OCEMOD: 101759

ARTICLE IN PRESS

Ocean Modelling xxx (xxxx) xxx

Contents lists available at ScienceDirect

Ocean Modelling

journal homepage: www.elsevier.com/locate/ocemod

Influence of anomalous low-level circulation on the Kuroshio in the Luzon Strait during ENSO

Yi-Chun Kuo, Yu-Heng Tseng *

Institute of Oceanography, National Taiwan University, Taipei, Taiwan

ARTICLE INFO

Keywords:
Kuroshio
Luzon Strait
ENSO
Mesoscale eddies

ABSTRACT

Basin-scale wind curl anomalies in the North Pacific associated with El Niño increase westward Kuroshio transport in the Luzon Strait, whereas those associated with La Niña reduce it. However, the Kuroshio current in the Luzon Strait is further affected by mesoscale eddies and local wind stress. Numerical experiments are conducted to demonstrate that the anomalous low-level circulation over the Philippine sea during El Niño weakens the northeasterly monsoon and favors the development of mesoscale eddies at the same time. This is caused by the increased baroclinic instability in the Subtropical Countercurrent (STCC)/North Equatorial Current region. Our results are supported by the long-term observational data. Consequently, the Kuroshio pattern in the Luzon Strait during El Niño tends to be more unsteady. During La Niña, the Kuroshio loop is enhanced in response to strengthened northeasterly winds. Furthermore, vorticity stretching, caused by local wind stress and associated curl anomalies during La Niña, contributes to the formation of a cyclonic eddy off the southeastern Taiwan.

1. Introduction

Situated to the south of Taiwan, the Kuroshio forms a loop in the Luzon Strait. Accompanying this current, the Pacific waters intrude into the South China Sea (SCS). This is important for the momentum, heat, and salt budgets of the SCS basin. Kuo and Tseng (2020) show that the enhanced Kuroshio intrusion during El Niño can modulate the upper and middle layer circulation of the northern SCS through changes of the planetary vorticity flux input from the Luzon Strait. An enhanced Kuroshio intrusion results in stronger eddy activity and more saline water in the northern SCS (Nan, 2015). Similar to the Loop Current in the Gulf of Mexico, multiple states of the Kuroshio have been demonstrated, such as penetration into the SCS, shedding eddies, or leaping the gap (Sheremet and Kuehl, 2007; Kuehl and Sheremet, 2009). Flow pattern dynamics in the Luzon strait have been extensively studied. Assuming a steady-state under PV conservation, the intruding flow path can be determined by the upstream flow condition (flow speed and direction) at the entrance of the strait (Hurlburt and Thompson, 1980; Xue et al., 2004). The vorticity balance is dominated by the advection and β terms. When the upstream Kuroshio speed is small enough, allowing β-effect to dominate flow motions, the Kuroshio intrudes westward into the northern SCS; when the flow inertia is strong enough, it leaps across the Luzon Strait (Sheremet and Kuehl, 2007; Kuehl and Sheremet, 2009).

The seasonal and intraseasonal variability of the Kuroshio intrusion is attributed mainly to monsoon winds, westward migrating mesoscale eddies, and variation in the North Equatorial Current (NEC) (Sun et al., 2019). A close relationship has been observed between the East-Asian monsoon and Luzon Strait transport into the SCS (Metzger and Hurlburt, 2001). However, wind-driven Ekman transport is small, accounting for less than 10% of all Luzon Strait transport (Qu et al., 2004). The monsoon winds are believed to alter Kuroshio intrusion by changing Kuroshio inflow angle or speed (Kuehl and Sheremet, 2009). The mesoscale eddies that propagate westward have a substantial influence on Kuroshio transport. These are generated in the Subtropical Countercurrent (STCC) region of the western Pacific as a result of baroclinic instability (Qiu, 1999). An anticyclonic (cyclonic) eddy can considerably increase (decrease) Kuroshio transport east of Taiwan (Chang et al., 2018). A cyclonic mesoscale eddy can increase the westward intrusion of the Kuroshio loop by reducing the upstream (to the west of Luzon Island) flow velocity. Zheng et al. (2011) suggest that eddies with a radius greater than 150 km are strong enough to substantially alter the Kuroshio and modify the local circulation pattern. Because the intruding path of the Kuroshio in the Luzon Strait is strongly correlated with its upstream flow (~16°N), its interactions with eddies to the east of Luzon island have more influence on flow path than interactions in downstream regions (Chang et al., 2015; Kuo et al., 2017). Moreover, the seasonal cycle of Kuroshio transport in the Luzon Strait is related to mesoscale eddies (Lien et al., 2014).

In terms of interannual timescales, the variation in Luzon Strait transport has been connected with El Niño-Southern Oscillation (ENSO)

* Corresponding author.
E-mail address: tsengyh@ntu.edu.tw (Y.-H. Tseng).

https://doi.org/10.1016/j.ocemod.2021.101759
Received 31 July 2020; Received in revised form 11 November 2020; Accepted 14 January 2021
Available online xxxx
1463-5003/

in many studies. Using Sverdrup dynamics without considering friction, the transport around an island can be estimated from the integration of basin wind stress (Island rule, Godfrey, 1989). On the basis of this island rule assumption, basin-scale ENSO-related wind stress anomalies may regulate the interannual variability of Luzon Strait transport. Wang et al. (2006) suggest that the westerly wind burst in the equatorial Pacific greatly influences Luzon Strait transport during El Niño events. The Kuroshio speed is strongly correlated with the meridional shift of NEC bifurcation, which is the origin of the Kuroshio and Mindanao Current (MC). The complicated NEC, Kuroshio, and MC system shows strong interannual variation dominated by the ENSO dynamic (Kim et al., 2004). During El Niño, the northward shift of the NEC bifurcation results in a stronger Mindanao Dome and weaker Kuroshio transport (Tozuka et al., 2002) whereas the situation is reversed during La Niña (Yaremchuk and Qu, 2004; Qu et al., 2004). Kim et al. (2004) suggest that this is mainly due to the westward propagation of upwelling (downwelling) Rossby waves generated by winds in the central equatorial Pacific, and by an anomalous anticyclone (cyclone) located in the western North Pacific when a warm (cold) event matures. Previous studies have primarily focused on the effects of basin-scale wind anomalies and remote effects from the tropics. However, dynamics of the flow pattern in the Luzon Strait are more complicated than these speculations.

In addition to the basin-scale forcing, the ENSO can substantially influence the regional wind pattern, which may further affect the Kuroshio in the Luzon strait. During El Niño, an anomalous cyclonic gyre in the low-level atmosphere is formed north of the equator. This is an atmospheric Rossby wave response to the heating anomaly in the central equatorial Pacific. The anomalous northerly to the west of the Rossby gyre advects low background moist enthalpy southward, creating an anomalous subsidence that further induces this anomalous low-level anticyclone over the Philippine Sea (Wang et al., 2000; Li et al., 2017). Anticyclonic wind anomalies in the western North Pacific typically develop rapidly during late autumn and then reach their mature phases in winter (December to February). The anomalous winds tend to reverse their signs during La Niña. Using a high-resolution regional coupled model, Kuo and Tseng (2020) suggest that the anomalous low-level anticyclone/cyclone during El Niño/La Niña can induce the mesoscale anomalies in the upper SCS, which can further feedback to the atmosphere through the energy exchange at the air–sea interface in the northern SCS (see their Fig. 9).

The influence of this anomalous low-level anticyclone/cyclone on the Kuroshio loop in the Luzon Strait has, however, rarely been investigated. Using sensitivity experiments, we explored the modulation of these ENSO-related wind anomalies on the flow pattern in the Luzon Strait. This is the first high-resolution coupled model used to investigate upper ocean variation in this region during ENSO events. As detailed in the result section, the influence of the basin-scale wind anomaly on Kuroshio transport across the Luzon strait was initially investigated using the long-term observational data (i.e., island rule). Then, the impact of regional wind anomalies on the flow pattern variation of the Luzon Strait was further examined through sensitivity experiments.

2. Model and reanalysis data

2.1. Model description and numerical experiments

The Coupled Ocean–Atmosphere–Wave–Sediment Transport modeling system (Warner et al., 2010) was used in this study. This is based on the weather research and forecasting (WRF) model, the regional ocean modeling system (ROMS), and the SWAN (Simulating WAves Nearshore) model. To emphasize the interaction between the ocean and the atmosphere, we only coupled ocean and atmosphere components and did not consider wave effects. Both WRF and ROMS use two two-way nested domains (Fig. 1). The horizontal resolutions for the first (outer) domain were 36 and 24 km for the WRF model and ROMS, respectively, whereas those for the second (inner) domain were 12 and 9 km, respectively (a third of the first domain). Vertically, 36 and 25 levels were used in the WRF model and ROMS, respectively. National Centers for Environmental Prediction (NCEP) Final (FNL) Operational Model Global Tropospheric Analyses data were used to determine the initial and lateral boundary conditions (updated every 6 h) for the WRF model. The ROMS uses realistic topography from the ETOPO2 (US Department of Commerce, National Oceanic and Atmospheric Administration, National Geophysical Data Center, 2006). Global 1/12° ocean predictions with the Hybrid Coordinate Ocean Model (HYCOM) or Navy Coupled Ocean Data Assimilation Analysis data were used as initial and lateral boundary conditions (updated every 10 days). Since our model grids, topography and the atmospheric forcing are different from those used in the HYCOM, gravity waves may be generated during the adjustment process. The coupled model effectively reaches its quasi-equilibrium state within a few days because of the small region and the low frequency update of the lateral boundary condition. This is confirmed by the time-series of volume averaged kinetic energy within the 9km inner domain (Figure not shown).

We chose two strongest ENSO events (in the decaying phases) in recent years (i.e., 2015/16 El Niño and 2011/12 La Niña). The El Niño simulation lasted from November 1, 2015, to June 30, 2016 (Exp. 0a), whereas the La Niña simulation lasted from November 1, 2011, to June 30, 2012 (Exp. 0b). Two more experiments were conducted to examine the different impacts of ENSO on the Kuroshio intrusion into the Luzon Strait (Table 1). Exp. 1a used 2011/12 WRF atmospheric forcing to drive 2015/16 ocean conditions. Exp. 1b used 2015/16 WRF (atmosphere) forcing to drive 2011/12 ocean conditions. To avoid the ocean feedback that would further modify the atmospheric conditions, the WRF model is forced by the same reference SST (6-hourly NCEP FNL data) in Exp. 0 and Exp. 1, and therefore the atmospheric forcing used to force the ROMS are essentially identical between Exp. 0 and Exp. 1.

2.2. Observation and reanalysis data

To characterize the effects of basin-scale wind anomalies on the Kuroshio intrusion in the Luzon Strait, 0.25° global monthly 10 m winds were retrieved from vector wind analyses using the Cross-Calibrated Multi-Platform (CCMP) version 2.0. The data are available at www.remss.com The data period spans from November 1989 to February 2016. In addition, the 10 m-wind of 0.25° ECMWF ERA5 reanalysis is used to calculate the Philippines–Taiwan Oscillation (PTO) index (Chang and Oey, 2012). The wind stress vector was calculated using the bulk formula in Large and Pon (1981).

The long-term upper ocean (0–50 m) eddy kinetic energy (EKE) data were analyzed using HYCOM + NCODA Global 1/12° Reanalysis (https://www.hycom.org/dataserver/gofs-3pt1/reanalysis). The NCODA uses a multivariate optimal interpolation scheme to assimilate available ocean observations (Cummings, 2006). The data set provides high-resolution daily global ocean states from January 1994 to December 2015. The model accurately describes the deep open ocean, shallow coastal areas, and the mixed layer (Chassignet etal, 2009).

We also used gridded (1/4° × 1/4°) monthly sea level anomalies (SLAs) to calculate surface EKE. The SLA data (based on the 1993–2012 mean, the annual cycle is not removed) comes from Ssalto/Duacs multimission altimeter products (http://www.aviso.altimetry.fr). The observed EKE was defined as $(u_g'^2 + v_g'^2)/2$, where u_g' and v_g' are the anomalies of zonal and meridional geostrophic velocities, respectively, as estimated from the Coriolis (f) and pressure balance of SSH anomalies (Hwang etal, 2004).

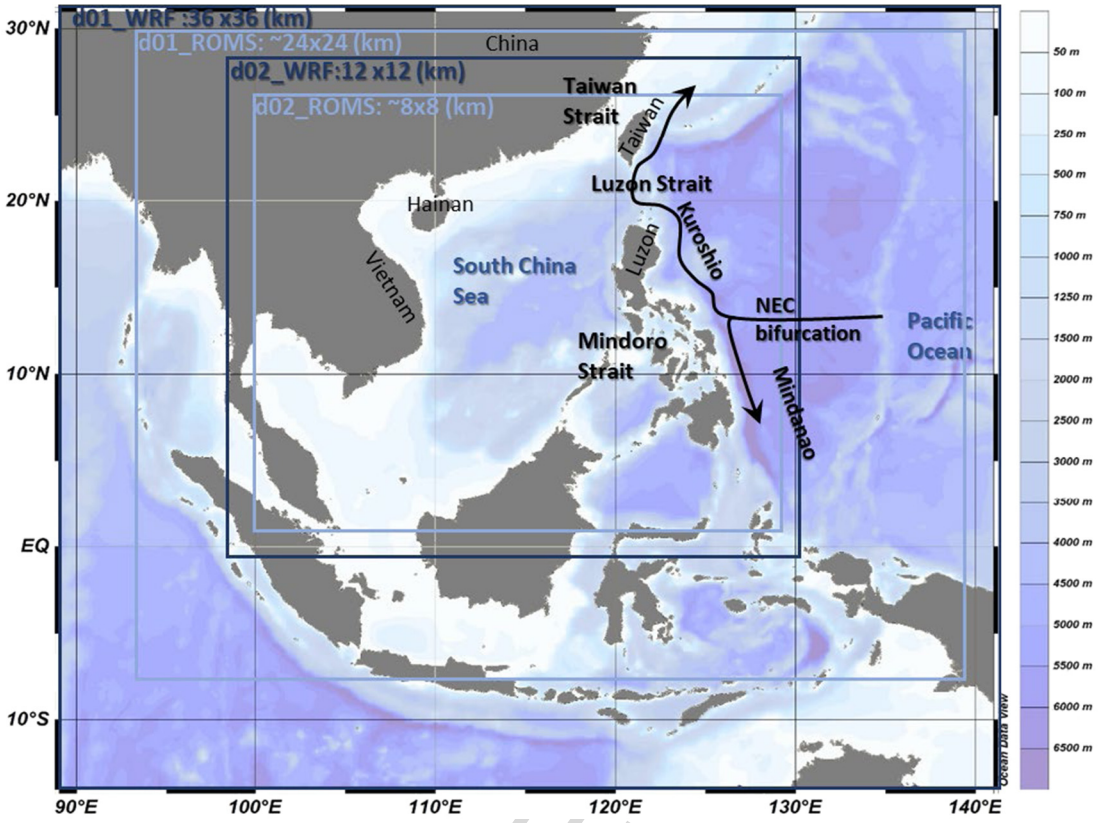

Fig. 1. Model domain setting and bottom topography (shaded).

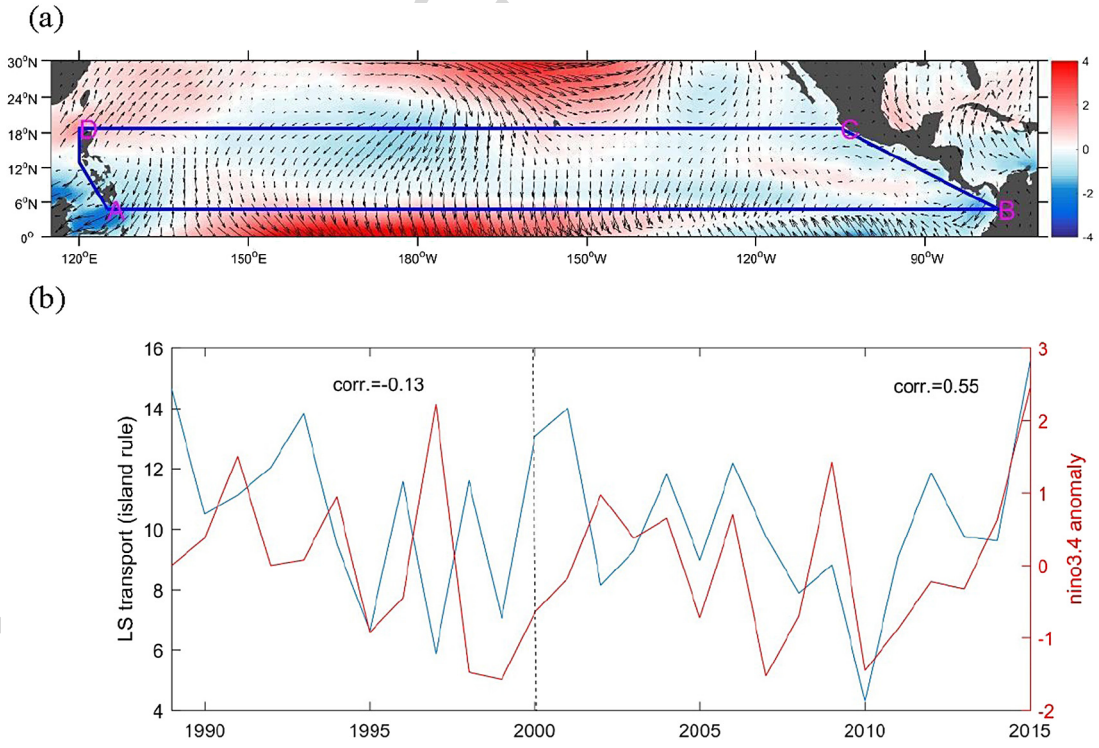

Fig. 2. (a) Composite difference in the zonal wind speed (m/s, shaded) and wind vector during winter (November to February) between six strong warm and cold ENSO phases (El Niño: 2006, 2009, and 2015; La Niña: 2007, 2010, and 2011). ABCD shows the locations used in Eq. (1). (b) Variation of T_0 (Sv) in Eq. (1) during winter from 1989 to 2016, calculated using CCMP data.

Table 1
Setting for experiments and the averaged EKE to the east of Luzon in each case.

	ROMS IC/BC	WRF IC/BC	EKE (cm^2/s^2) (16–20° N, 124–128° E)	EKE (cm^2/s^2) perturbed I.C. (16–20° N, 124–128° E) IC 1/ IC 2
Exp. 0a	2015/11–2016/2	2015/11–2016/2	502	511/493
Exp. 0b	2011/11–2012/2	2011/11–2012/2	352	386/385
Exp. 1a	2015/11–2016/2	2011/11–2012/2	465	473/476
Exp. 1b	2011/11–2012/2	2015/11–2016/2	394	423/412

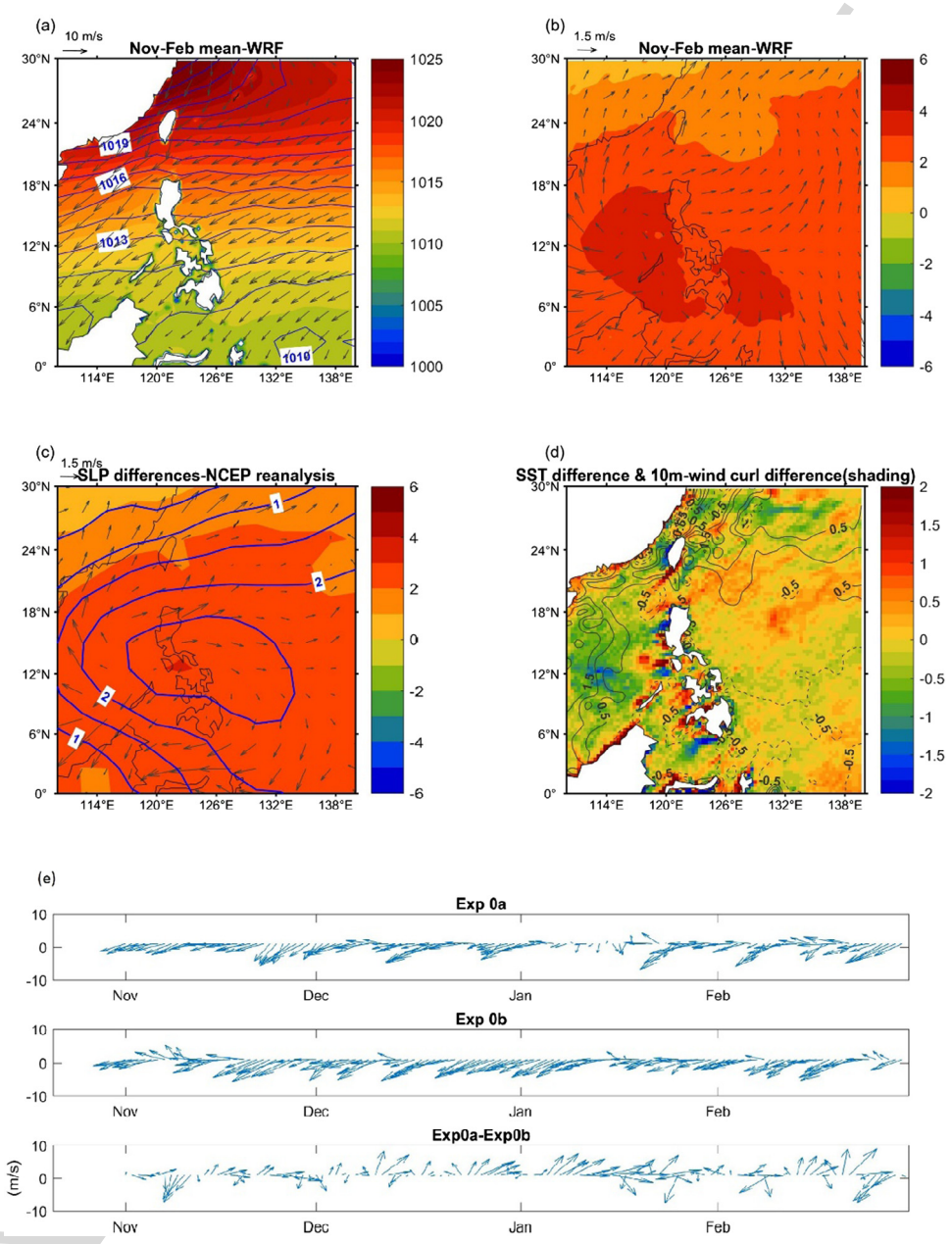

Fig. 3. (a) Modeled sea surface winds and sea level pressure (shading) during the 2015/16 El Niño winter. The sea level pressure from NCEP reanalysis is superimposed (black contours). (b) Modeled sea surface winds and sea level pressure differences between Exp0a and Exp0b. (c) Same as (b) but from NCEP reanalysis. The blue contours show composite difference of sea level pressure from 6 recent ENSO years (El Niño: 2006, 2009 and 2015; La Niña: 2007, 2010 and 2011). (d) Difference in SST (°C, contours) and 10m-wind curl ($x10^{-5}s^{-1}$, shading) in WRF between Exp0a and Exp0b. (e) The wind vectors time series averaged over a box region shown in (a) in Exp. 0a, Exp. 0b and the difference.

3. Results

3.1. Basin-scale forcing associated with ENSO

Metzger and Hurlburt (1996) suggest that the mean Kuroshio intrusion in the Luzon Strait is primarily a function of Pacific basin-scale forcing and model geometry in the Sulu Sea. The Luzon Strait, Mindoro Strait, and Sibutu Strait in the Sulu Sea in the vicinity of the Philippines make it a geometrically isolated island in the Pacific (Qu et al., 2000). Godfrey (1989) calculated the alongshore pressure gradient that drives model geostrophic western boundary currents against friction using Sverdrup theory (i.e., the island rule). The island rule is derived from

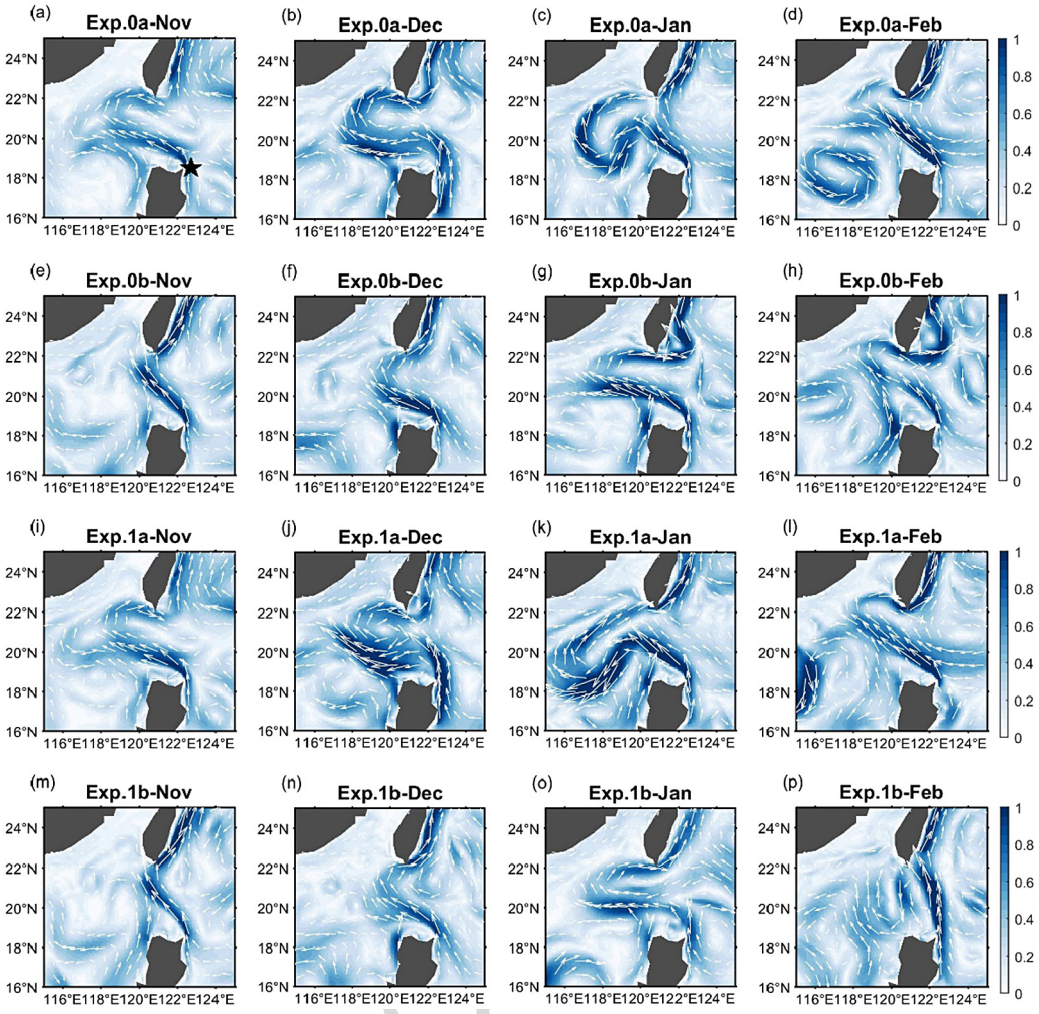

Fig. 4. Monthly mean current pattern (0–50 m, unit: m/s) in the Luzon Strait in (a)–(d) Exp. 0a, (e)–(h) Exp. 0b, (i)–(l) Exp. 1a and (m)–(p) Exp. 1b. The star mark in (a) shows the location (18.5°N -19°N, 122.5°E -123°E) of the momentum budget analysis in Fig. 6.

the momentum balance between vorticity input by wind curl, the flux of planetary vorticity, and frictional dissipation along the western boundary. Using the continuity equation, the island rule expresses the circulation around an island in terms of wind stress.

$$T_0 = \frac{1}{f_D - f_A} \oint_{ABCD} \frac{\tau^{(l)}}{\rho_0} dl \quad (1)$$

Monthly 10 m winds (CCMP version 2.0) and Eq. (1) are used to estimate Luzon Strait transport based on Sverdrup dynamics with negligible friction (Godfrey, 1989). The surface wind stress vector T is calculated using the bulk formula, $T = \rho_a C_d U_{10} \boldsymbol{U}_{10}$, where ρ_a is air density, U_{10} is 10-m height wind speed, and C_d is the drag coefficient determined by Large and Pon (1981). The locations of A to D are shown in Fig. 2a. AB and CD are located along 4.75°N and 18.75°N, respectively.

The interannual changes of T_0 relate more closely to the wind variation along AB and CD than along BC and DA (Wang et al., 2006). When El Niño is developing, westerly and easterly anomalies in the central and eastern region along AB and easterly anomalies along CD considerably modify T_0 in Eq. (1). Wang et al. (2006) found that these basin-scale wind anomalies modify the Kuroshio transport lead the Nino3.4 index by 6 months, suggesting the role of summer T_0 on the mature of ENSO. Fig. 2a shows winter (November–February) composite zonal wind anomalies in recent six warm and cold ENSO phases (El Niño: 2006, 2009, 2015; La Niña: 2007, 2010, 2011). Hereafter, winter is represented based on the months of November–February. During the El Niño warm phase, an anticyclone and a cyclone are formed in the western and central tropical northern Pacific, respectively. These are the typical El Niño matured features (Tseng et al., 2017). Fig. 2b further shows the winter variation of T_0 from 1989 to 2016 (mean water transport is approximately 10.3 Sv, with a standard deviation of 2.7 Sv). The simultaneous winter Niño3.4 anomalies (1981–2010 climatology removed) are superimposed in Fig. 2b (source: https://psl.noaa.gov/gcos_wgsp/Timeseries/Nino34/). Their simultaneous correlation over the entire period is insignificant (approximately 0.23). However, the correlation was significantly increased after 2000 (correlation = 0.55, significant at 95% confidence). Hu et al. (2017) suggested that a northwestward shift of air–sea coupling is associated with Bjerknes feedback (Bjerknes, 1969) after 2000, which results from enhanced ocean–atmosphere coupling in the Northern Hemisphere (Ding et al., 2017; Hu and Fedorov, 2018). Bjerknes feedback is a positive feedback from large-scale oceanic and atmospheric circulations over the tropical Pacific. These consistencies confirm that the northward shift of zonal wind anomalies associated with SST coupling caused most of the ENSO warm events after 2000 and enhanced the relationship between ENSO and Luzon Strait transport estimated by the island rule (which is based on the region ABCD). We note that the island rule assumes a steady-state and idealized ocean. However, in reality, Kuroshio intrusion is unsteady (Metzger and Hurlburt, 2001) and fully nonlinear, which means that other dynamic effects, such as mesoscale eddies, are far from negligible.

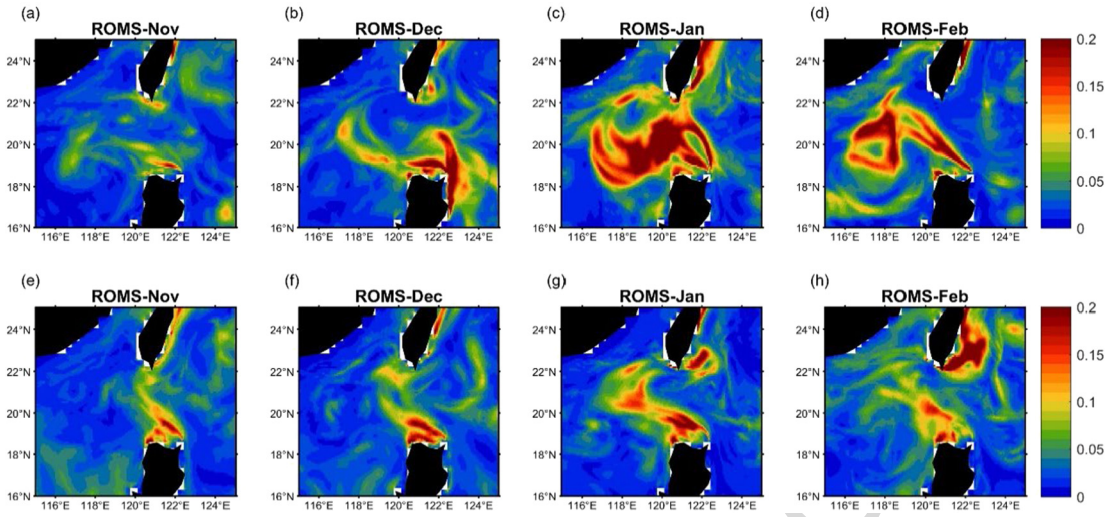

Fig. 5. Current speed monthly variance (0–50 m, unit: m^2/s^2) in (a)–(d) Exp. 0a and (e)–(h) Exp. 0b. The monthly variance $S \equiv u'^2 + v'^2, u' = u - \overline{u}, v' = v - \overline{v}$, u' (v') and $\overline{u}(\overline{v})$ are the daily and monthly mean velocities, respectively.

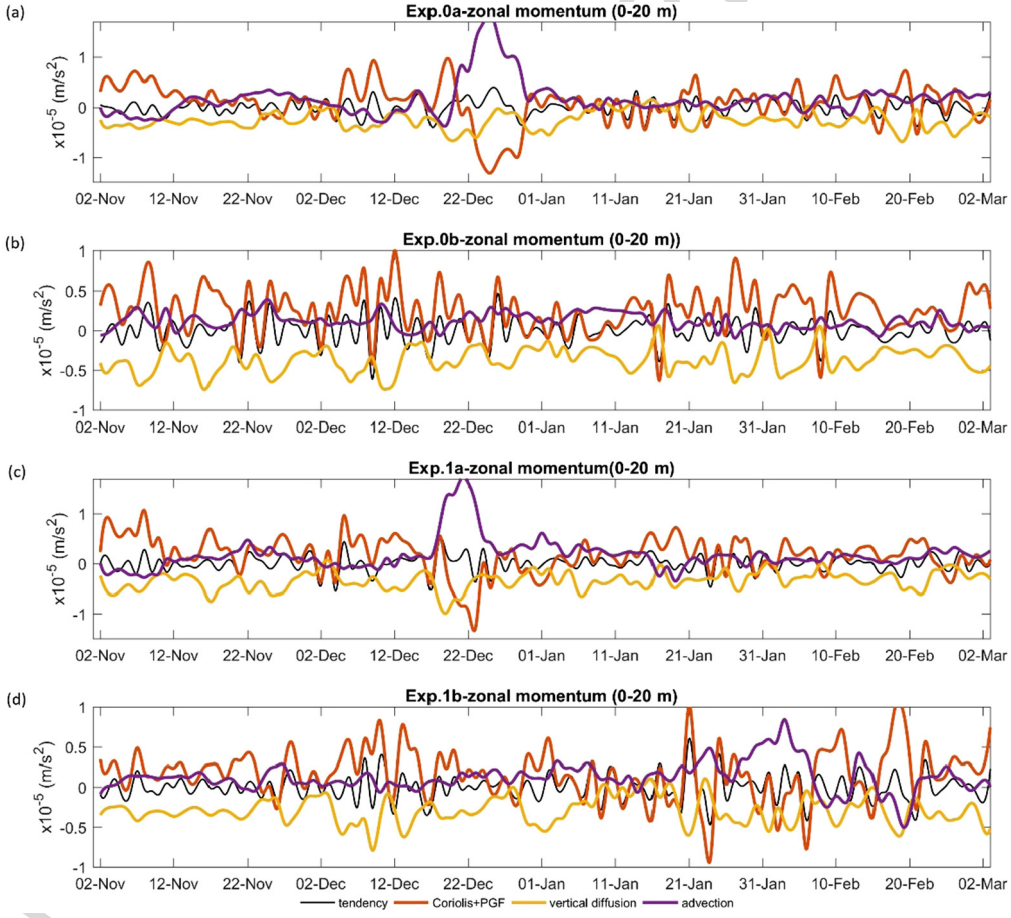

Fig. 6. January–February momentum balance in the upstream region (18.5°N -19°N, 122.5°E -123°E, the star mark in Fig. 4a) of Kuroshio in (a) Exp. 0a, (b) Exp. 0b, (c) Exp. 1a and (d) Exp. 1b.

3.2. Numerical model results

3.2.1. Difference in low-level atmospheric condition between El Niño and La Niña

Fig. 3a shows the modeled low-level winds (black vectors) and sea level pressure (shading) during the 2015/16 El Niño winter (November–February) superimposed by the NCEP reanalysis. The modeled pattern is similar to the NCEP reanalysis except that in this case the modeled sea level pressure is slightly higher in the northern region (>22°N). Fig. 3b shows the average winter difference between the 2015/16 El Niño and the 2011/12 La Niña. Anomalous high pressure, associated with an anticyclonic circulation, occurs around the SCS

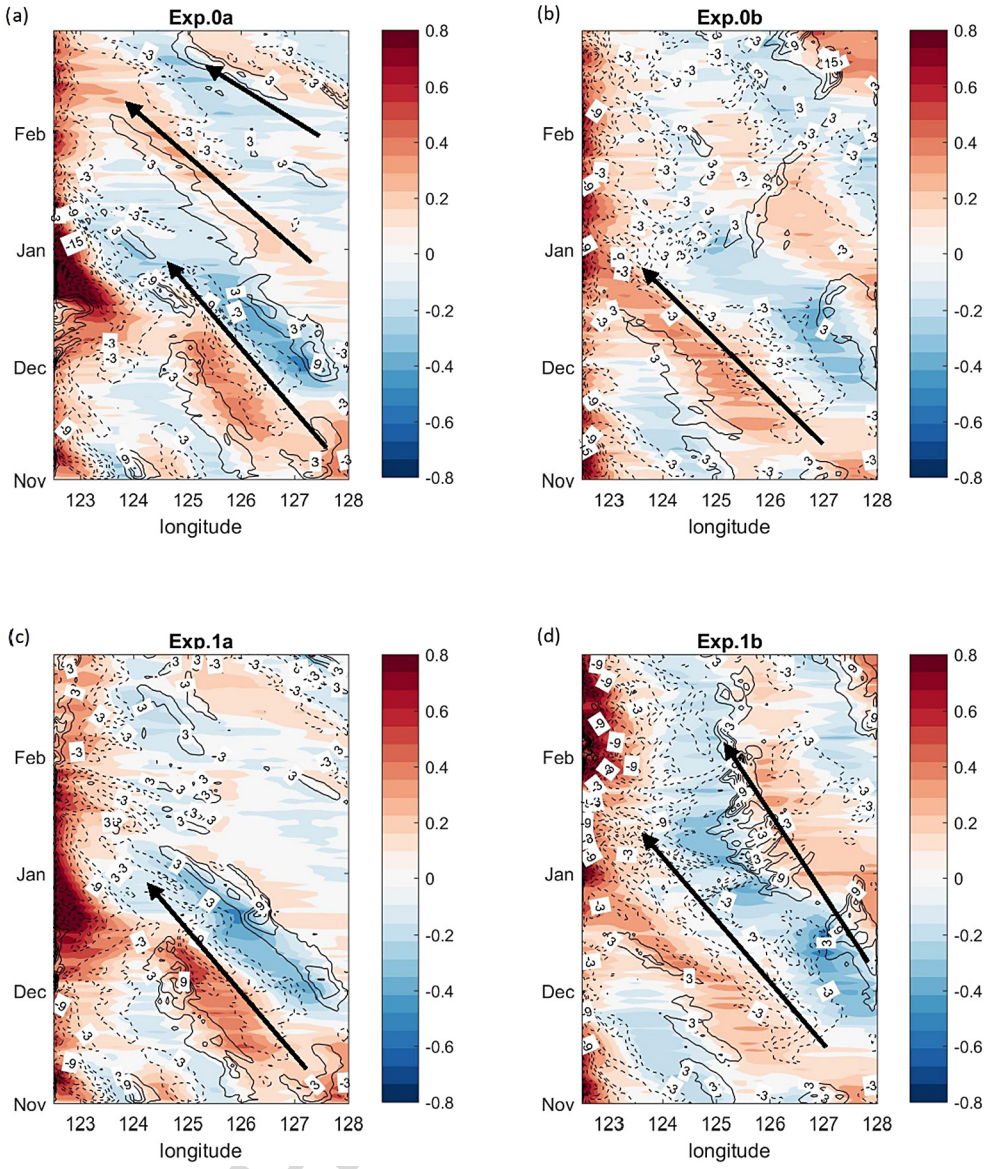

Fig. 7. Hovmöller diagram of meridional velocity (color, m/s) and relative vorticity (contours, contour interval: 3 × $10^{-6}s^{-1}$), averaged between 16° and 20°N in the four experiments. The black arrows mark the westward propagation signals.

and east of the Philippines. In the Luzon Strait, the anomalous southwesterly weakens the typical northeasterly monsoon. This is a general feature in all ENSO years. The composite difference in sea level pressure from six recent ENSO years (El Niño: 2006, 2009, 2015; La Niña: 2007, 2010, 2011) is also superimposed in Fig. 3c (blue contours) and shows similarly anomalous high pressure. Sverdrup dynamics suggest that anomalous winds in the northwestern Pacific can modify the western boundary current speed and change the Kuroshio state in the Luzon Strait accordingly.

The wind vector time series at the center of the Luzon Strait is presented in Fig. 3e. These confirm that the northeasterly monsoon is larger during La Niña than El Niño, especially during December to February. Moreover, the northeasterly wind is relatively steady during La Niña, whereas the wind direction changes rapidly during El Niño. This large variation suggests an increase in the occurrence of inertial motions in the ocean.

3.2.2. The ocean responses

Fig. 4 compares the 0–50 m monthly mean current pattern in the Luzon Strait. In November, the current speed (shaded in Fig. 4) is weaker and the westward Kuroshio intrusion is more considerably during El Niño (Exp. 0a). This intrusion is then enhanced until January regardless of ENSO phase (Exp. 0a and Exp. 0b). During La Niña (Exp. 0b), the current off southeastern Taiwan exhibits a cyclonic circulation that is commonly observed in winter (Hsin et al., 2010) and driven by the northeast monsoon. In Exp. 1a, the 2011/12 atmospheric condition (i.e., La Niña atmospheric condition) was used to drive the 2015/16 ocean initial and boundary conditions used in Exp. Compared with Exp. 0a, Exp. 1a shows a stronger Kuroshio current speed and enhanced intrusion into the SCS (see Fig. 4a). This results directly from stronger monsoon wind forcing (i.e., Fig. 3c) that enhances the Kuroshio loop (Kuehl and Sheremet, 2009). Under both the influence of mesoscale eddy and strong wind forcing, the loop current severely deformed and an anticyclonic eddy was shed from the Kuroshio current (Fig. 4k-l). On the other hand, in Exp. 1b, the 2015/16 atmospheric condition was used (El Niño atmospheric condition) to drive the 2011/12 ocean initial and boundary conditions. The cyclonic circulation off the southeastern coast of Taiwan shown in Fig. 4g–h is now absent. This cyclonic circulation is discussed further in the next section. Additionally, a leaping current replaces the loop current in the Luzon Strait during

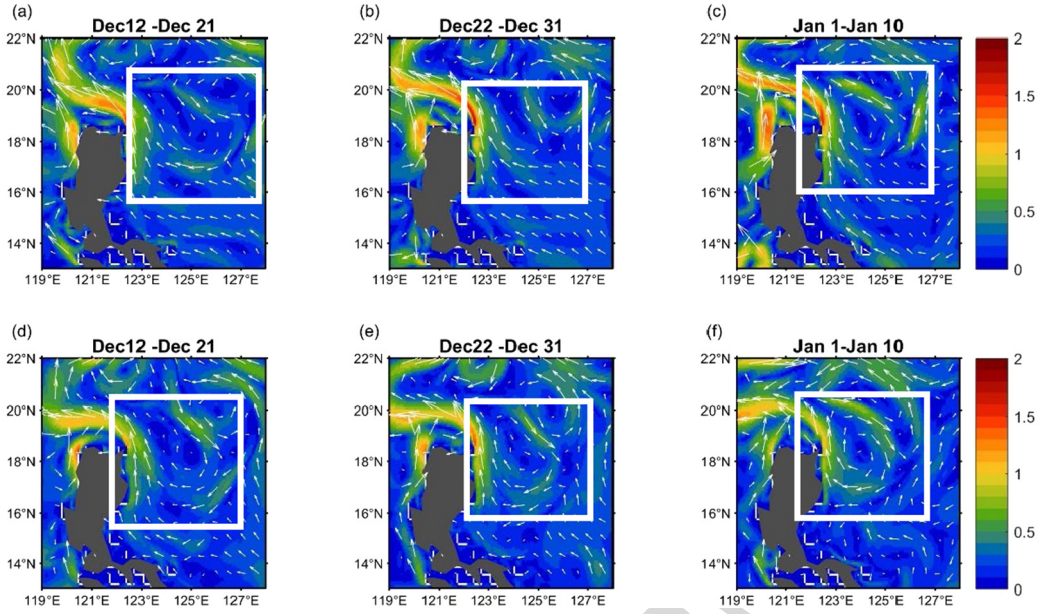

Fig. 8. 10-day averaged flow field (0–10 m) between 2011/12/22 and 2012/1/10 in (a)–(c) Exp0b and (d)–(f) Exp1b. Color shading indicates flow speed (m/s). The white rectangles mark the evolution of an anticyclonic eddy.

February associated with an enhanced anticyclonic eddy (will be shown in the following), accompanying a stronger upstream Kuroshio off the eastern and northeastern coast of Luzon Island.

The 0–50 m current speed monthly variance in Exp. 0 is further compared in Fig. 5 (current speed monthly variance $S \equiv u'^2 + v'^2, u' = u - \overline{u}, v' = v - \overline{v}$, $u'\overline{u}'$ and $v'\overline{v}'$ are the daily and monthly mean velocity, respectively). As expected, the monthly variance in the Luzon Strait is much weaker during La Niña. The locations of monthly maximum velocity variance also differ in these ENSO years. During El Niño, the upstream Kuroshio variation is prominent in December, as a result of which the loop current becomes unsteady in the ensuing months. During La Niña, the current state off southeastern Taiwan significantly changes from January to February (Fig. 5b) as the cyclonic circulation forms.

To further investigate the relevant flow dynamics in the Luzon Strait, Fig. 6 compares the zonal momentum budget (at 10 m depth) in the Strait (20°N, 120.5°E) during January to February. Both Exp. 0a and Exp. 0b show an enhanced Kuroshio loop and unsteady features. The zonal momentum equation is as follows:

$$\overbrace{\frac{\partial u}{\partial t}}^{tendency} \cong \underbrace{-\vec{u}\cdot\nabla u}_{advection} + \overbrace{fv}^{Coriolis} - \underbrace{\frac{1}{\rho_0}\frac{\partial P}{\partial x}}_{PGF} + \overbrace{\frac{\partial}{\partial z}\left(K_{Mv}\frac{\partial u}{\partial z}\right)}^{vertical\ diffusion} \quad (2)$$

Where K_{Mv} is the vertical viscosity coefficient. The horizontal diffusion is negligible. The ageostrophic velocity component is represented by the summation of the Coriolis and pressure gradient force (PGF) terms. Our analysis suggests that the advection term dominates the variation in zonal ageostrophic velocity more frequently in Exp. 0a (Fig. 6a), whereas the diffusion term dominates the momentum variation in Exp. 0b (Fig. 6b). This infers that upstream Kuroshio variation or eddy activities dominate momentum change during El Niño (Exp. 0a), whereas wind stress forcing dominates during La Niña (Exp. 0b). This is consistent with the local wind difference shown in Fig. 3e. The local wind during La Niña is much stronger and steadier. In Exp. 1a (Fig. 6c), the diffusion term shows a more dominant role comparing to Exp. 0a due to a stronger and steadier local wind during the La Niña. In Exp. 1b (Fig. 6d), the advection term is enhanced especially during Jan–Feb, implying a more unsteady condition due to the nonlinear interactions between the mean flow and perturbations.

To show upstream Kuroshio variation and the zonally propagating features that play an important role in the Luzon Strait flow pattern, we present a Hovmöller diagram of meridional velocity and relative vorticity averaged between 16° and 20°N in Fig. 7. The Kuroshio is located around 122°E to 123°E. In the case of an El Niño event (Exp. 0a), the upstream Kuroshio speed greatly increases during December due to propagating eddies/Rossby waves. The westward-propagating features (mesoscale eddies) are stronger during El Niño than La Niña. Kuroshio speed is significantly modulated by these propagating features. In Exp. 1a, the westward-propagating signals become weaker under La Niña local atmosphere forcing (comparing Fig. 7c with Fig. 7a) and stronger under El Niño atmosphere forcing (comparing Fig. 7d with Fig. 7b). To further illustrate the spatial structures of these differences, Fig. 8 compares the 10-day averaged flow field (0–10 m) between 2011/12/22 and 2012/1/20 in Exp0b and Exp1b. An anticyclonic circulation appears to the east of Luzon in both runs. It grows through January and became a stronger eddy during 1/11–1/20. Comparing these two runs, the circulation speed of the anticyclonic eddies in Exp. 1b is stronger. Note that the wind curl difference between Exp. 1b and Exp. 0b during this period is positive, indicating the vorticity input from wind forcing cannot well explain the enhancement of the anticyclonic eddy. We quantify the variations of mesoscale eddies energy using EKE in these experiments. As expect, The upper 50 m mean EKE for the region of 16–20°N and 124°E–128°E (Table 1) in Exp0a (502 cm^2/s^2) is much larger than that in Exp. 0b (352 cm^2/s^2). The mean EKE in the same region is 465 and 394 (cm^2/s^2) in Exp. 1a and Exp. 1b, respectively. Compared to the control runs (Exp0), when the 2015/16 El Niño atmosphere forcing is replaced by the 2011/12 La Niña forcing, the EKE is decreased. Reversely, when the 2011/12 La Niña atmosphere forcing is replaced by the 2015/16 El Niño forcing, the EKE is increased. These results suggest that anomalous winds in the western North Pacific might be responsible for the stronger westward propagating eddy activities to the east of the Kuroshio.

Since internal variability commonly exists in the ocean model arising from its nonlinearity (Penduff et al., 2011), particularly in the regions with vigorous mesoscale eddy activities, we further perform 8 additional ensemble simulations (2 for each experiment) to confirm the

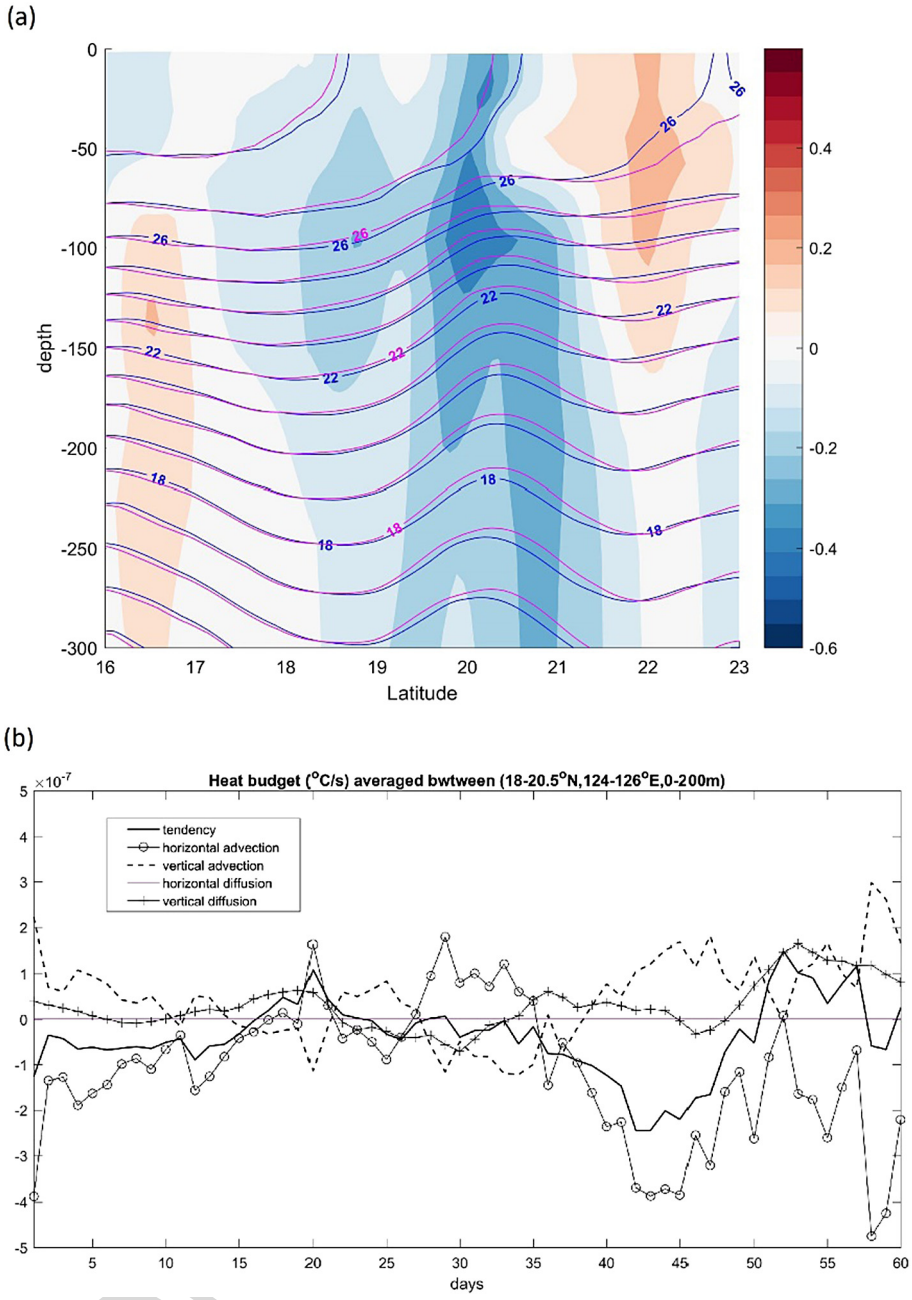

Fig. 9. (a) Isotherm in Exp. 0b (°C, blue contours) and Exp. 1b (°C, magenta contours) averaged between 124°E and 126°E. The temperature difference between Exp. 0b and Exp. 1b is color shaded (°C). (b) The heat budget (°Cs^{-1}, Eq. (3)) difference, averaged between 0–200 m in the front zone region (18–20.5°N), between Exp. 1b and Exp. 0b.

model consistency. We perturb the initial temperature field at the first model level by a Gaussian distributed random number generator (mean of zero and standard deviation of 0.5 °C) (Table 1) as the independent random noise for the ensembles, similar to Turner et al. (2008) and Yin et al. (2011). This value of standard deviation is chosen because the Remote Sensing Systems (www.remss.com) suggested that the accuracy for the AMSR-E (The Advanced Microwave Scanning Radiometer for EOS) Ocean Products is approximately 0.5 °C and the advanced very high resolution radiometer (AVHRR) nonlinear SST algorithm (NLSST) error characteristics is also 0.5 °C (Nalli and Smith, 1998). These additional ensembles show consistent decrease/increase relation discussed earlier (Table 1) while the internal variability arising from the nonlinearity in ocean is relatively small compared to the difference between Exp1 and Exp0.

Figs. 4–8 confirm that the flow monthly variance during the El Niño is stronger and primarily caused by the oceanic advection associated with mesoscale eddies. During the La Niña, flow monthly variance is mostly caused by local wind stress (Fig. 6). Qiu and Chen (2010) analyzed long-term satellite altimeter data and found that the generation of mesoscale eddies on the STCC region is associated with wind-induced convergence that modifies the temperature gradient as well as the vertical shear of the upper ocean current in the frontal region. Thus, the anomalous negative wind curl may enhance mesoscale eddies propagating westward to the east of Kuroshio. We further explored the impacts of different ENSO-related atmospheric forcing on the upper ocean in two additional experiments. Long-term observation data were also analyzed in the present study to support our conclusions. Qiu and Chen (2010) explained interannual variation in the kinetic

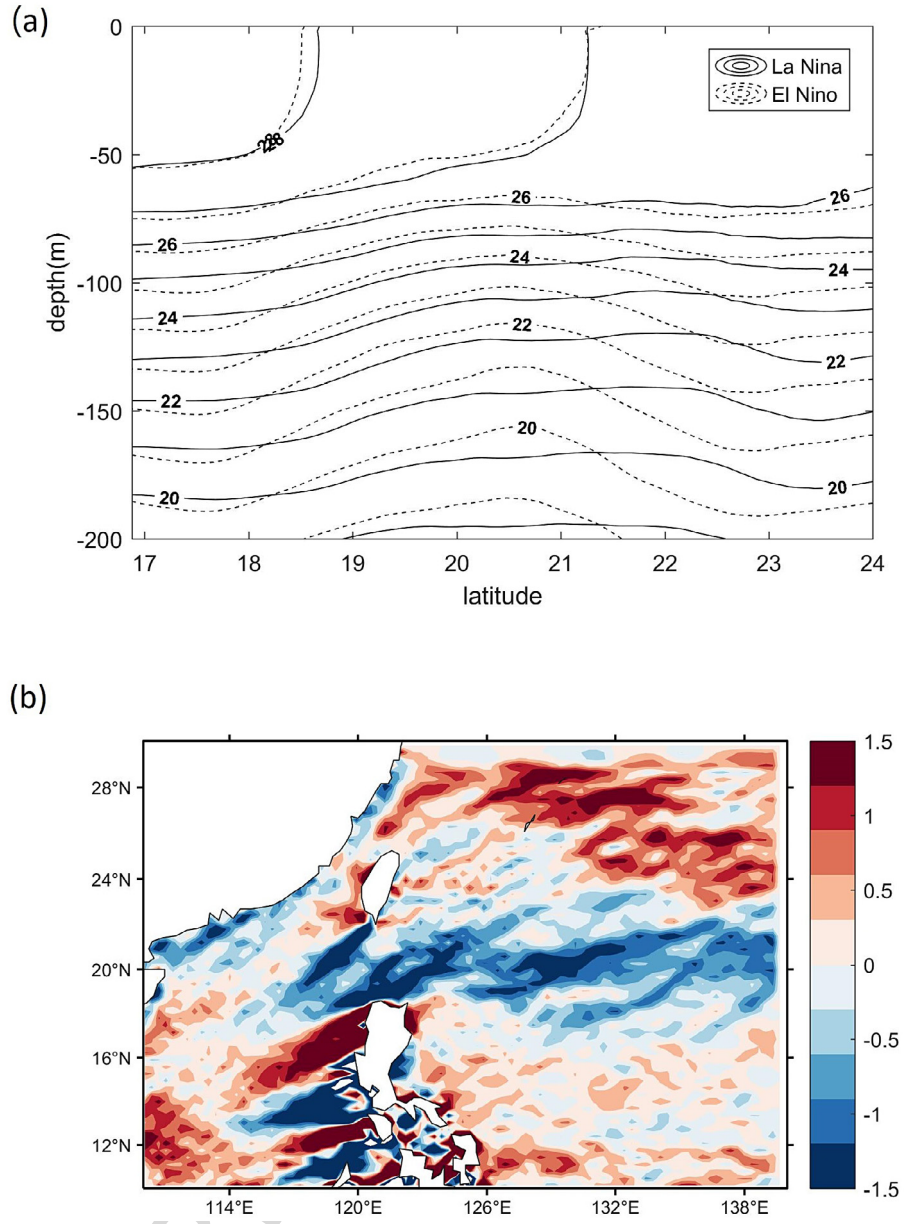

Fig. 10. (a) Composite result of isotherm (°C) averaged between 124°E and 126°E during the El Niño winters and La Niña winters using HYCOM reanalysis (GOFS 3.1). El Niño: 1997/98, 2002/03, 2009/10, 2015/16; La Niña: 1999/00, 2007/08, 2010/11, 2011/12. (b) difference of $\frac{\partial v_{Ek}}{\partial y}$ ($x10^{-3}s^{-1}$) between Exp. 0a and Exp. 0b. v_{Ek} is the meridional Ekman velocity.

energy level of eddies in the STCC band (18°N–25°N) based on varying surface Ekman temperature gradient convergence. $\frac{\partial G}{\partial t} \cong -\frac{\partial (v_{Ek} G)}{\partial y}$, where G is the meridional temperature gradient ($-\partial T/\partial y$) and $v_{Ek} = -\tau^x/\rho f H$ is the meridional Ekman velocity. According to 2011/12 initial ocean and boundary conditions, El Niño-related anomalous winds (i.e., atmospheric low-level anticyclonic high-pressure anomalies) in the Philippine Sea (Exp. 1b) alter the thermocline slope, leading to increased baroclinic instability in the STCC-NEC region. Hence, the eddies in Exp1b are stronger than those caused by the 2011/12 La Niña atmospheric forcing in Exp. 0b. This is supported by Fig. 9(a), which shows that isotherms in the front zone (16°N–22°N, zonally averaged between 124°E and 126°E) become steeper in Exp. 1b compared with Exp. 0b. The temperature difference between Exp. 0b and Exp. 1b is also shaded. Cooling occurred at the cold side of the front, with a larger change from 0 to 100 m. This caused the isotherms between 17°N and 20°N to tilt upward (0 to 200 m). Similar characteristics to Figs. 7–9 can be found in the additional ensemble mean (see the Appendix).

To further support the thermocline change in the front region shown in Fig. 9(a), the heat budget (Eq. (3)) difference between Exp. 1b and Exp. 0b is plotted in Fig. 9(b). This is averaged between 0 and 200 m in the front zone region, where cooling occurs with the tilted isotherms shown in Fig. 10(a).

$$\frac{\partial T}{\partial t} + u\frac{\partial T}{\partial x} + v\frac{\partial T}{\partial y} + w\frac{\partial T}{\partial z} + \frac{\partial}{\partial z}\left(k\frac{\partial T}{\partial z}\right) + \nabla A_h \nabla T = 0 \quad (3)$$

The budget is primarily dominated by the horizontal advection, which is caused by the anomalous Ekman transport associated with easterly wind anomalies. The vertical diffusion is mostly positive. The reduced wind speed in Exp. 1b compared with Exp. 0b, associated with anticyclonic circulation anomalies (Fig. 3b), causes smaller upward latent heat flux in the ocean surface and weaker subsurface turbulent mixing. In summary, the above heat budget analysis shows that the

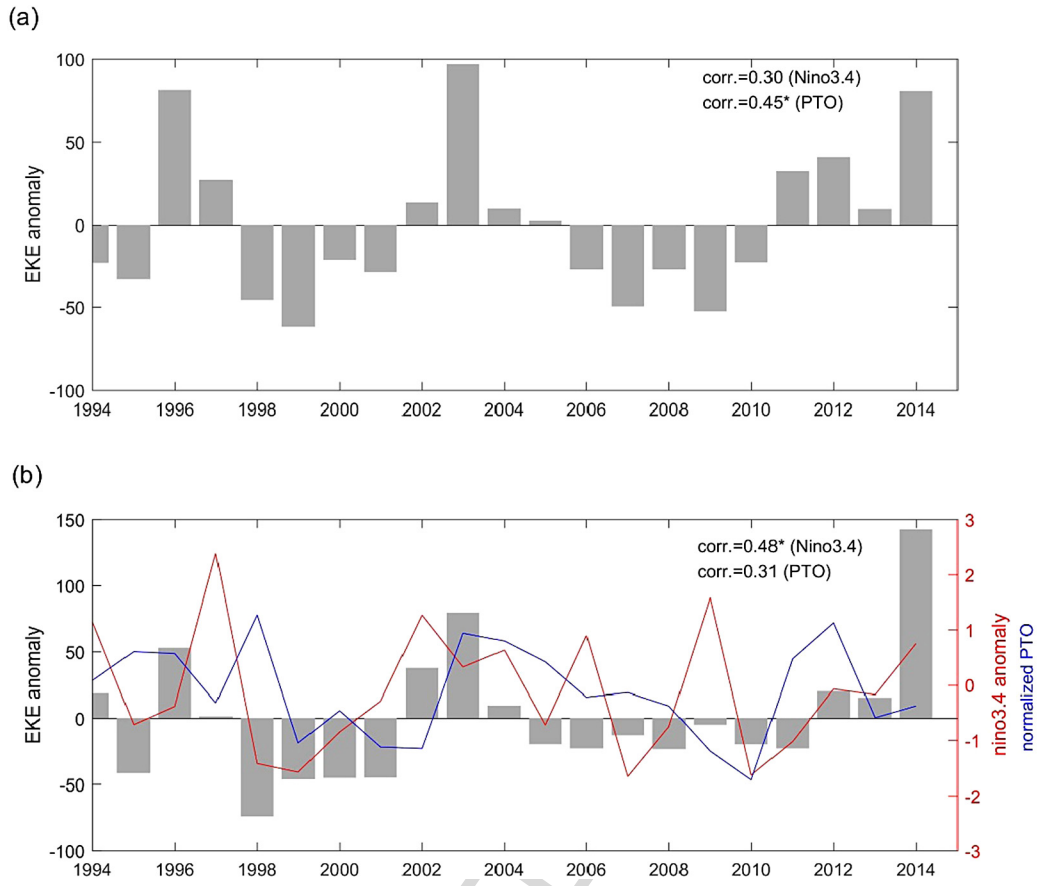

Fig. 11. Mean EKE anomalies (cm^2/s^2,0–50 m) (November–February) based on HYCOM Global 1/12° reanalysis data (https://www.hycom.org/dataserver/gofs-3pt1/reanalysis) in two regions. (a) To the east of Taiwan (22–28°N,125–140°E) and (b) to the east of Luzon (14–20°N, 125–140°E). Their correlations with Niño3.4 (November–February) and normalized PTO (March–June, 8-mon lead, based on Chang and Oey (2012)) are also listed. Correlations significant at the 95% confidence level using Student's t test are marked with "*".

anomalous winds, rather than the surface heat fluxes, dominate the isotherm tilting process in the upper ocean (Chow et al., 2017).

The wind anomalies associated with El Niño induce Ekman convergence, which enhances the horizontal temperature gradient in this region, strengthening velocity shear and baroclinic instability. On the basis of the simple linear theory of baroclinic instability (Phillips, 1954), the stable condition for a two-layer model is $|\Delta U| \leq 2\beta_0 g' H / f_0^2$, where ΔU is the velocity shear between the two layers, f_0 and β_0 are the Coriolis and beta parameters in the beta plane approximation, H is the total water depth, and g' is the reduced gravity. The upward tilting of the isotherms in the front region (17.5–21°N) in Exp. 1b compared with Exp. 0b indicate a stronger current shear. Moreover, greater cooling occurred in the upper layers (0 to 100 m) than in the lower layers (100 to 200 m) [Fig. 10(a)]. This suggests a weaker density difference between the upper and lower layers and thus a smaller Rossby deformation radius in Exp1b. These differences can lower the baroclinic unstable condition criteria and effectively enhance baroclinic instability to generate more mesoscale eddies (Chow et al., 2017). Fig. 10(a) shows the composite of isotherm averaged between 124°E and 126°E during 8 ENSO events (El Niño: 1997/98, 2002/03, 2009/10, 2015/16; La Niña: 1999/00, 2007/08, 2010/11, 2011/12), using the HYCOM reanalysis data (GOFS 3.1). The results confirm that the meridional temperature gradient is larger during El Niño. Our model results suggest that the anomalous local wind stress may contribute to this difference, however, it requires further study for possible remote effects and is beyond the scope of this work.

Fig. 10b shows the differences in meridional gradient of v_{Ek} between Exp. 0a and Exp. 0b (Exp. 0a–Exp. 0b), in the western Pacific; positive values to the south of 17°N, and negative between 17°N–20°N, respectively. This implies the spatially varying impacts of the anomalous wind forcing on the ocean thermal structure, consistent with previous studies in terms of different ENSO effects on the STCC.

3.2.3. Analysis of observational data and other indices

White et al. (1978) found that interannual variation of the subtropical front associated with the STCC is linked to ENSO signals. However, Qiu and Chen (2010) found that, rather than the Niño-3.4 index, the negative West Pacific teleconnection (WP) index correlated better with Ekman forcing over the STCC. During the negative phase of the WP pattern, anomalous low pressure increases Ekman transport convergence in the STCC band, which causes an enhanced thermocline tilt of the STCC. Variation of Kuroshio in the Luzon Strait due to mesoscale eddies greatly depends on location of interaction between the Kuroshio and eddies. When this occurs in the upstream region (i.e., to the east of Luzon Island), the Kuroshio state can change drastically from leaping to looping (or eddy shedding). However, when the eddy–Kuroshio interaction occurs in the northern half of the Luzon Strait or to the east of Taiwan, the Kuroshio state in the Luzon Strait is less influential (Kuo et al., 2017). Therefore, an ENSO-related anomalous low-level anticyclone (cyclone) located in the Philippine Sea or eastern SCS region may play an important role in Kuroshio variation in the Luzon Strait due to the impingement of westward-migration mesoscale eddies.

To confirm these modeled features, Fig. 11 shows long-term mean surface EKE (November to February) based on the HYCOM + NCODA

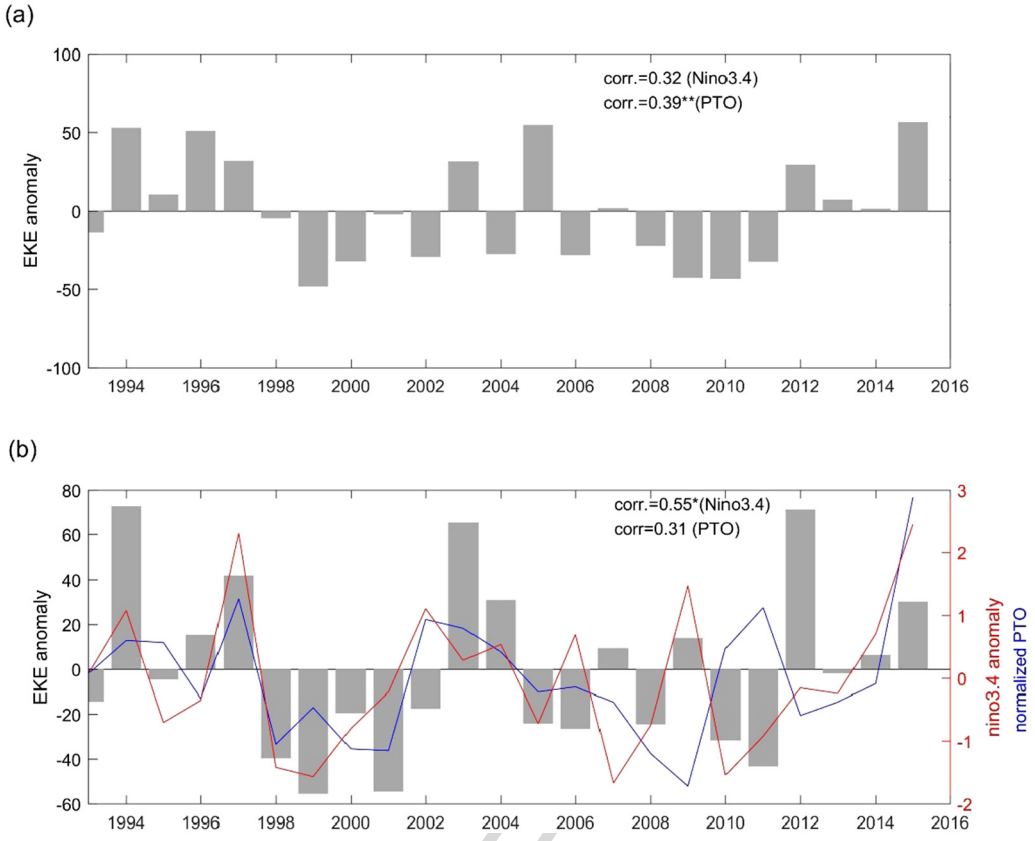

Fig. 12. Same as in Fig. 11 except that gridded absolute dynamic topography data (http://www.aviso.altimetry.fr) are used. Correlations significant at the 95% and 90% confidence level using Student's t test are marked with "*" and "**" respectively.

Global 1/12° reanalysis. Niño3.4 index was significantly correlated with the mean surface EKE anomalies in the region to the east of Luzon (14–20°N, 125–140°E, correlation coefficient = 0.48, significant at the 95% confidence) but not in the region to the east of Taiwan (21–26°N, 125–140°E, correlation coefficient = 0.3). Similar results can be found in the EKE anomalies estimated using the AVISO data (Fig. 12). The correlation coefficient is significantly higher to the east of Luzon Island (0.55, significant at the 95% confidence) than east of Taiwan (correlation coefficient = 0.32) in the AVISO data. On the other hand, the PTO index (Chang and Oey, 2012), directly associated with the wind stress curl changes in the western North Pacific, seems to correlate better with the EKE east of Taiwan (correlation coefficient = 0.45, significant at the 95% confidence) than to the east of Luzon Island (correlation coefficient = 0.31, insignificant) at approximately 6–9 months lead time (Fig. 11, March to June average is superimposed). This is also confirmed in Fig. 12 but the correlation is lower. Chang and Oey (2012) showed that positive PTO connects well with the larger EKE in the region of 123–140°E and 18–25°N (correlation coefficient = 0.76, their Fig. 1a), northern displacement of NEC and the larger Kuroshio intrusion into the SCS. The inconsistent relationship of the EKE with PTO and ENSO is unclear but may be due to the different active regions of the wind stress anomalies. The winds associated with PTO are around 140–180°E, while the ENSO related anomalous low-level anticyclone locates further southwestward and is closer to the Luzon and the South China Sea region.

3.2.4. Cyclonic circulation off the southeastern Taiwan coast

Fig. 13 shows the wind curl difference (contours) and 0–50 m averaged vorticity difference (shading) between El Niño (Exp. 0a) and La Niña (Exp. 0b). Except for the southwest coast of Taiwan, the wind stress curl during winter in the vicinity of Taiwan is generally positive (Jan et al., 2015). The wind curl difference shows a different spatial distribution from the typical winter pattern, suggesting a reduced vorticity input from wind stress forcing during El Niño. In the vicinity of the southwestern coast of Taiwan, the sign for wind curl difference is the same as that for upper-ocean vorticity difference, confirming the contribution of vorticity input from the atmospheric winds to the ocean. In the case of La Niña, cyclonic circulation to the southeast of Taiwan appears in January, the generation or maintenance of which is assisted by concurrent negative wind curl anomalies.

This cyclonic circulation is absent in Exp. 1b (Fig. 8) but present in Exp. 0b (Fig. 5). The atmospheric wind differences are responsible for this absence. Fig. 14 shows the upper 50-m vorticity budget (Eq. (1)) during January in Exp. 0b. The dominant terms are stretching and advection. The meridional and zonal advection terms almost balance each other. Consequently, the wind-induced local flow convergence increases the stretching term and development of cyclonic circulation. In addition to the local wind effect, an enhanced and steady Kuroshio loop associated with the La Niña wind anomaly results in stronger eastward current off the southern tip of Taiwan that can strengthens the horizontal convergence (the stretching term).

$$\overbrace{\frac{\partial \zeta}{\partial t}}^{tendency} + \overbrace{u\frac{\partial \zeta}{\partial x}}^{zonal\ adv.} + \overbrace{v\frac{\partial \zeta}{\partial x}}^{meridional\ adv.} + \overbrace{(\zeta + f)\ \nabla \cdot \vec{u}}^{stretching} + \overbrace{v\frac{\partial f}{\partial y}}^{betaterm} - \overbrace{\frac{g}{\rho^2}\left(\frac{\partial \rho}{\partial x}\frac{\partial}{\partial y}\int_z^0 \rho dz - \frac{\partial \rho}{\partial y}\frac{\partial}{\partial x}\int_z^0 \rho \rho dz\right)}^{baroclinic\ term} - \overbrace{\nu\frac{\partial^2 \zeta}{\partial^2 z}}^{diffusion} = 0 \quad (4)$$

4. Conclusion

During an El Niño developing stage, westerly wind anomalies occur in the equatorial Pacific. Wang et al. (2006) suggested that these basin-scale wind anomalies modify the Kuroshio transport through the

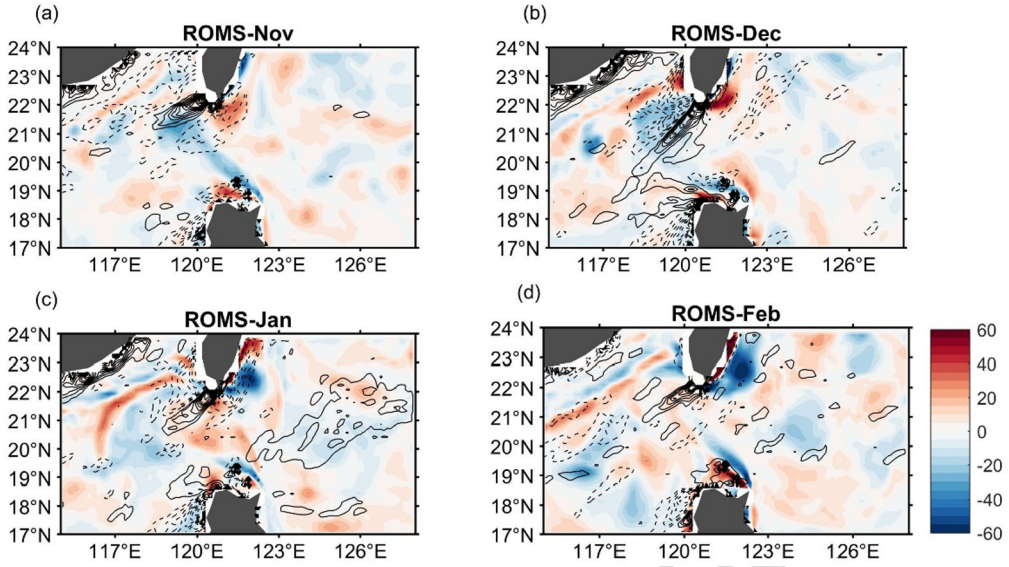

Fig. 13. Wind stress curl difference (black contours, interval: 5 × 10^{-7}Nm^{-3}) and averaged vorticity difference (x10^{-6}s^{-1}, shading) over the upper 50 m between Exp. 0a and Exp. 0b (the former minus the latter) in (a) November, (b) December, (c) January, and (d) February.

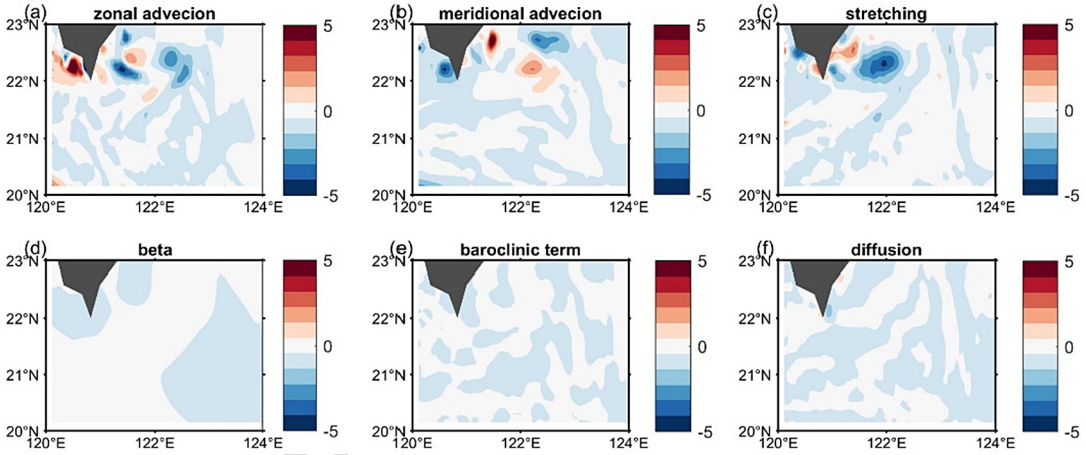

Fig. 14. Vorticity budget (x10^{-10} s^{-2}) in Eq. (3) for the upper 50 m during January in Exp. 0b.

Sverdrup dynamic and the basin-scale winds driven Luzon strait transport anomaly is found leading the Niño3.4 index by 6 months. Using the island rule (Godfrey, 1989), we confirmed that the simultaneous connection between winter matured ENSO index and the winter Kuroshio intrusion was significantly increased after 2000, possibly explained by the northwestward shift of air–sea coupling after 2000 which results mainly from the enhanced ocean–atmosphere coupling in the Northern Hemisphere. In addition, an anomalous anticyclone over the South China Sea and Philippine Sea rapidly develops in late autumn and then matures in winter during ENSO events. These regional wind anomalies further modulate the Kuroshio in the Luzon Strait on the top of the basin-scale wind background effects.

Model sensitivity experiments show that during El Niño, westward propagating mesoscale eddies to the east of Kuroshio are enhanced due to increased baroclinic instability caused by the Ekman convergence in the front zone and a weaker density difference vertically that lowers the baroclinic unstable condition criteria. In the meantime, the anomalous southwesterly in the Luzon Strait weakens the typical northeasterly monsoon. Consequently, the Kuroshio pattern in the Luzon Strait during El Niño tends to be more unsteady. During La Niña, the Kuroshio loop is enhanced in response to the strengthened northeasterly winds. These enhanced wind stresses and the associated wind stress curl favor the development of a cyclonic eddy off the southeastern Taiwan.

Overall, the basin-scale wind anomalies induce the oceanic responses (mainly Sverdrup dynamics), resulting in the change of Luzon strait transport associated with Rossby waves generated during the adjustment process. The regional anticyclonic wind anomalies produce horizontal convergence in the frontal region which further enhances baroclinic instability. The former process (i.e., basin-scale wind anomalies) is barotropic and can be approximately as the steady state. However, the latter process (regional anticyclonic wind anomalies) is baroclinic, which includes strong nonlinearity that can only be resolved in the high-resolution model simulation.

In the present study, we focus on the direct ocean response to different atmospheric forcing associated with ENSO events. In our sensitivity experiments, the local air–sea interaction is simplified to a one-way process that excludes the influence of ocean feedback. The feedback to the atmosphere resulting from the oceanic response may introduce complexity (Kuo and Tseng, 2020). Specifically, the strong nonlinearity associated with the ocean mesoscale feature may force the above atmosphere through the air–sea heat exchange process. Consequently, the resulting modulation of the low-level atmosphere

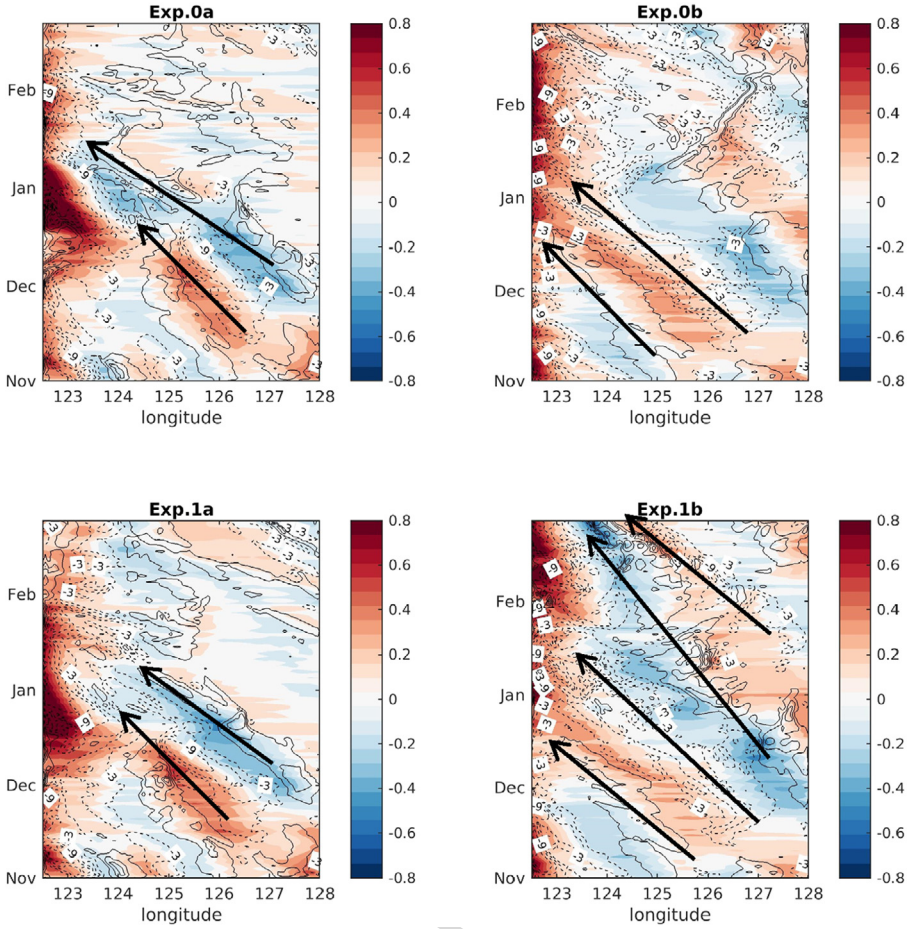

Fig. A.1. Same as Fig. 7 except from the averaged of two I.C. perturbed experiment (referred to Table 1).

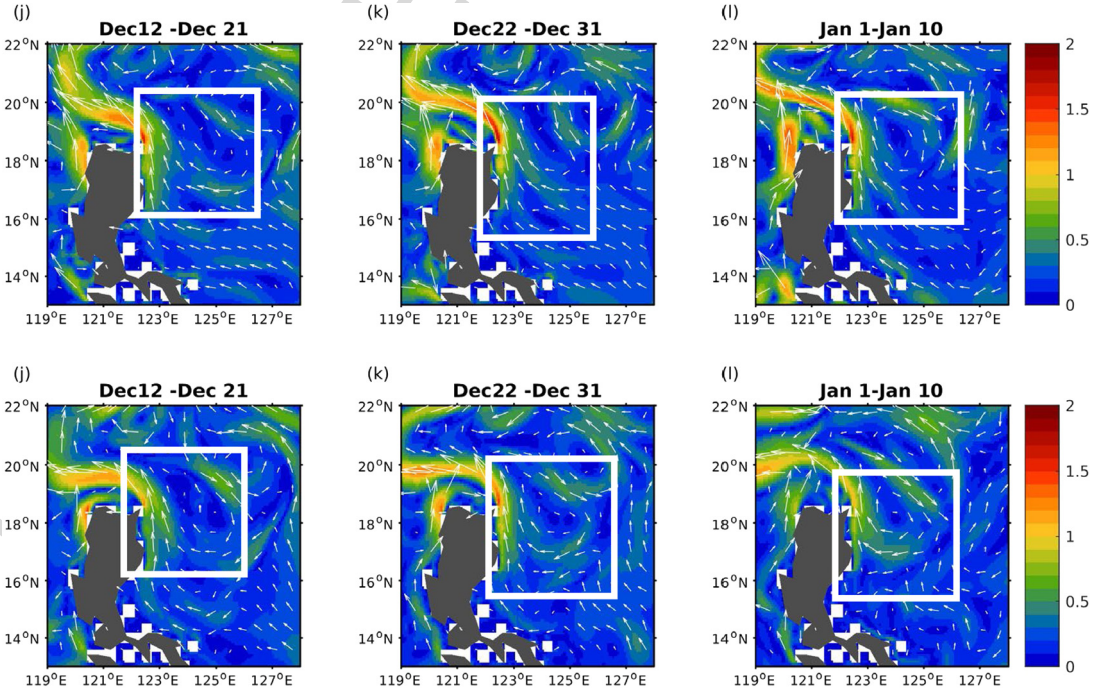

Fig. A.2. Same as Fig. 8 except from the averaged of two I.C. perturbed experiment (referred to Table 1).

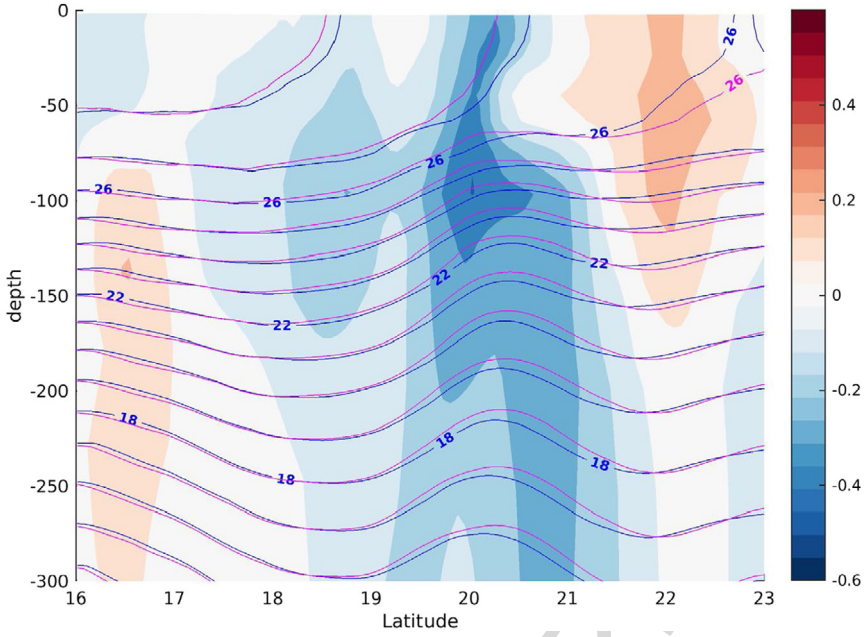

Fig. A.3. Same as Fig. 9(a) except from the averaged of two I.C. perturbed experiment (referred to Table 1).

may not be negligible. Further study to assess the contribution of this ocean feedback is required in the follow-up study.

CRediT authorship contribution statement

Yi-Chun Kuo: Formal analysis, Methodology, Writing - original draft. **Yu-Heng Tseng:** Conceptualization, Methodology, Writing - original draft.

Declaration of competing interest

The authors declare that they have no known competing financial interests or personal relationships that could have appeared to influence the work reported in this paper.

Uncited references

Chang (2004), Kim et al. (2014)

Acknowledgments

Constructive comments from the anonymous reviewers are greatly appreciated. The 1/12 deg global HYCOM+NCODA Ocean Reanalysis was funded by the US Navy and the Modeling and Simulation Coordination Office. Computer time was made available by the DoD High Performance Computing Modernization Program. The output is publicly available at http://hycom.org. Financial support by the MOST Grant 107-2611-M-002-013-MY4 and 108-2111-M-002-006-MY3, Taiwan, is appreciated.

Appendix

The mean EKE difference between the experiments and the unperturbed experiments varied from $-9 cm^2/s^2$ to $34 cm^2/s^2$ (Table 1), with an averaged difference of $16.6 cm^2/s^2$. These values are smaller than the deviations from the unperturbed experiment for Exp0b and Exp1b (both having the same 2011/12 ROMS I.C. 2011/12), showing the intrinsic internal variability associated with the initial perturbation is smaller than the forced dynamics as expected. Figs. A.1–A.3 show very similar results to the corresponding Figs. 7–9 based on the perturbed initial condition experiments. Note that the intensity difference of the westward propagating signals between Exp0a and Exp1a is not clear. This suggests the initial perturbation may interact with the wind forcing effects with similar magnitudes. However, the larger mean EKE and vertical thermal profile changes between Exp0a and Exp1a confirm the stronger baroclinic instability under the wind forcing change.

References

Bjerknes, J., 1969. Atmospheric teleconnections from the equatorial Pacific. Mon. Weather Rev. 97, 163–172.
Chang, C.P., 2004. East Asian Monsoon, vol. 2. World Scientific.
Chang, M.H., Jan, S., Mensah, V., Andres, M., Rainville, L., Yang, Y.J., Cheng, Y.H., 2018. Zonal migration and transport variations of the Kuroshio east of Taiwan induced by eddy impingements. Deep Sea Res. I 131, 1–15.
Chang, Y.L., Miyazawa, Y., Guo, X., 2015. Effects of the STCC eddies on the Kuroshio based on the 20-year JCOPE2 reanalysis results. Prog. Oceanogr. 135, 64–76.
Chang, Y.L., Oey, L., 2012. The Philippines–Taiwan oscillation: Monsoonlike interannual oscillation of the subtropical–tropical western north Pacific wind system and its impact on the ocean. J. Clim. 25, 1597–1618. http://dx.doi.org/10.1175/JCLI-D-11-00158.1.
Chow, C.H., Tseng, Y.H., Hsu, H.H., Young, C.C., 2017. The interannual variability of the subtropical countercurrent's eddies in the North Pacific associated with the Western- Pacific teleconnection pattern. Cont. Shelf Res. 143, 175–184.
Ding, R.Q., Li, J.P., Tseng, Y.H., Sun, C., Zheng, F., 2017. Linking a sea level pressure anomaly dipole over North America to the central Pacific El Niño. Clim. Dynam. 49, 1321–1339.
Godfrey, J.S., 1989. A Sverdrup model of the depth-integrated flow for the world ocean allowing for island circulations. Geophys. Astrophys. Fluid Dyn. 45 (1–2), 89–112.
Hsin, Y.C., Qu, T., Wu, C.R., 2010. Intra-seasonal variation of the Kuroshio southeast of Taiwan and its possible forcing mechanism. Ocean Dyn. 60 (5), 1293–1306.
Hu, S., Fedorov, A.V., 2018. Cross-equatorial winds control El Niño diversity and change. Nature Clim. Change 8, 798–802.
Hu, Z.Z., Kumar, A., Zhu, J., Huang, B., Tseng, Y.H., Wang, X., 2017. On the shortening of the lead time of ocean warm water volume to ENSO SST since 2000. Sci. Rep. 7, 4294.
Hurlburt, H.E., Thompson, J.D., 1980. A numerical study of Loop Current intrusions and eddy shedding. J. Phys. Oceanogr. 10 (10), 1611–1651.
Jan, S., Yang, Y.J., Wang, J., Mensah, V., Kuo, T.H., Chiou, M.D., Chern, C.S., Chang, M.H., Chien, H., 2015. Large variability of the Kuroshio at 23.75 N east of Taiwan. J. Geophys. Res.: Oceans 120 (3), 1825–1840.
Kim, Y.Y., Qu, T., Jensen, T., Miyama, T., Mitsudera, H., Kang, H.-W., Ishida, A., 2004. Seasonal and interannual variations of the North Equatorial Current bifurcation in a high-resolution OGCM. J. Geophys. Res. 109, C03040. http://dx.doi.org/10.1029/2003JC002013.
Kim, J.W., Yeh, S.W., Chang, E.C., 2014. Combined effect of El Niño-Southern Oscillation and Pacific decadal oscillation on the East Asian winter monsoon. Clim. Dyn. 42 (3–4), 957–971.

Kuehl, J.J., Sheremet, V.A., 2009. Identification of a cusp catastrophe in a gap-leaping western boundary current. J. Mar. Res. 67 (1), 25–42.
Kuo, Y.C., Chern, C.S., Zheng, Z.W., 2017. Numerical study on the interactions between the Kuroshio current in the Luzon Strait and a mesoscale eddy. Ocean Dyn. 67 (3–4), 369–381.
Kuo, Y.-C., Tseng, Y.H., 2020. Impact of ENSO on the South China Sea during ENSO decaying winter-spring modeled by a regional coupled model (a new mesoscale perspective). Ocean Model. 152, 101655.
Large, W.G., Pon, S., 1981. Open ocean momentum flux measurements in moderate to strong winds. J. Phys. Oceanogr. 11, 324–336.
Li, T., Wang, B., Wu, B., Zhou, T., Chang, C.P., Zhang, R., 2017. Theories on formation of an anomalous anticyclone in western North Pacific during El Niño: A review. J. Meteorol. Res. 31 (6), 987–1006.
Lien, R.C., Ma, B., Cheng, Y.H., Ho, C.R., Qiu, B., Lee, C.M., Chang, M.H., 2014. Modulation of Kuroshio transport by mesoscale eddies at the Luzon Strait entrance. J. Geophys. Res.: Oceans 119 (4), 2129–2142.
Metzger, E.J., Hurlburt, H.E., 1996. Coupled dynamics of the South China sea, the Sulu sea, and the Pacific ocean. J. Geophys. Res.: Oceans 101 (C5), 12331–12352.
Metzger, E.J., Hurlburt, H.E., 2001. The nondeterministic nature of Kuroshio penetration and eddy shedding in the South China Sea. J. Phys. Oceanogr. 31 (7), 1712–1732.
Nalli, N.R., Smith, W.L., 1998. Improved remote sensing of sea surface skin temperature using a physical retrieval method. J. Geophys. Res. 103, 10527–10542.
Penduff, T., Juza, M., Barnier, B., Zika, J., Dewar, W.K., Treguier, A.-M., Molines, J.-M., Audiffren, N., 2011. Sea level expression of intrinsic and forced ocean variabilities at interannual time scales. J. Clim. 24, 5652–5670. http://dx.doi.org/10.1175/JCLI-D-11-00077.1.
Qiu, B., 1999. Seasonal eddy field modulation of the North Pacific subtropical countercurrent: TOPEX/POSEIDON observations and theory. J. Phys. Oceanogr. 29, 2471–2486.
Qiu, B., Chen, S., 2010. Interannual-to-decadal variability in the bifurcation of the North Equatorial Current off the Philippines. J. Phys. Oceanogr. 40 (11), 2525–2538.
Qu, T., Kim, Y.Y., Yaremchuk, M., Tozuka, T., Ishida, A., Yamagata, T., 2004. Can Luzon Strait transport play a role in conveying the impact of ENSO to the South China Sea? J. Clim. 17 (18), 3644–3657.
Qu, T., Mitsudera, H., Yamagata, T., 2000. Intrusion of the north Pacific waters into the South China Sea. J. Geophys. Res.: Oceans 105 (C3), 6415–6424.
Sheremet, V.A., Kuehl, J., 2007. Gap-leaping western boundary current in a circular tank model. J. Phys. Oceanogr. 37 (6), 1488–1495.
Sun, B., Chen, Z., Wang, B., Wu, L., 2019. Seasonal variation of the North Equatorial Current bifurcation in regional model: Role of open boundary conditions. Ocean Model. 101528.
Tozuka, T., Kagimoto, T., Masumoto, Y., Yamagata, T., 2002. Simulated multiscale variations in the western tropical Pacific: The Mindanao Dome revisited. J. Phys. Oceanogr. 32 (5), 1338–1359.
Tseng, Y.H., Ding, R., Huang, X.-M., 2017. The warm blob in the northeastern Pacific-the bridge leading to the 2015/16 El Niño. Environ. Res. Lett. 12, 054019.
Turner, M.R.J., Walker, J.P., Oke, P.R., 2008. Ensemble member generation for sequential data assimilation. Remote Sens. Environ. 112 (4), 1421–1433.
Wang, D., Liu, Q., Huang, R.X., Du, Y., Qu, T., 2006. Interannual variability of the South China Sea throughflow inferred from wind data and an ocean data assimilation product. Geophys. Res. Lett. 33 (14).
Wang, B., Wu, R., Fu, X., 2000. Pacific-East Asian teleconnection: how does ENSO affect east Asian climate? J. Clim. 13, 1517–1536.
Warner, J.C., Armstrong, B., He, R., Zambon, J.B., 2010. Development of a coupled ocean–atmosphere–wave–sediment transport (COAWST) modeling system. Ocean Model. 35 (3), 230–244.
Xue, H., Chai, F., Pettigrew, N., Xu, D., Shi, M., Xu, J., 2004. Kuroshio intrusion and the circulation in the South China Sea. J. Geophys. Res.: Oceans 109 (C2).
Yaremchuk, M., Qu, T., 2004. Seasonal variability of the large-scale currents near the coast of the Philippines. J. Phys. Oceanogr. 34 (4), 844–855.
Yin, X., Qiao, F., Shu, Q., 2011. Using ensemble adjustment Kalman filter to assimilate Argo profiles in a global OGCM. Ocean Dyn. 61 (7), 1017–1031.
Zheng, Q., Tai, C.K., Hu, J., Lin, H., Zhang, R.H., Su, F.C., Yang, X., 2011. Satellite altimeter observations of nonlinear Rossby eddy–Kuroshio interaction at the Luzon Strait. J. Oceanogr. 67 (4), 365–376.